Faraday Discussions

SUPPLEMENTARY INFORMATION

Probing Interfacial Vibrations with IR Absorption Spectroscopy: from Molecular to Mesoscopic and Macroscopic Surfaces

Ashley M. Stingel,[a] Bashar Moussa,[a] Lilian Najm Alsayed,[a] Dennis K. Hore,[b] Poul B. Petersen*[a]

IR-ATR Solvation Shell Spectroscopy

Here we provide further considerations when designing and carrying out IR solvation shell spectroscopy in order to obtain high-quality and reliable solvation shell spectra.

Theoretical Considerations: Penetration and probing depth

To better understand penetration of the probe beam electric field from the incident electromagnetic wave into the bulk phase, we first consider that the absorbance is roughly proportional to the dot product between the macroscopic transition dipole moment

$$M = \sum_{\text{molecules}} \mu$$

and the ratio of the local field $E_{\text{loc}}(z)$ to the incident field E_0[1–3]

$$A \propto \left\langle M \cdot \frac{E_{\text{local}}}{E_0} \right\rangle^2 .$$

In isotropic media, there are three primary means by which the local field above the ATR crystal is altered: through an evanescent wave that decays exponentially into the refracted medium, through absorption (which also results in an exponential decay), and through multiple beam interference phenomena where transmitted and reflected waves interfere in the region of the molecules of interest. We start by considering the two simpler scenarios, where the interface exists between two semi-infinite media. The mean squared electric fields can be described by:[4–7]

$$\frac{\langle E_y(z)\rangle^2}{\langle E_y(z=-\infty)\rangle^2} = \left| t_s \exp\left[-\frac{2\pi z}{\lambda} Im(N_2 \cos\theta_2) \right] \right|^2$$

where $N_2 = n_2 + i\kappa_2$. Note that when $\kappa_2 > 0$, the refracted angle θ_2 becomes complex-valued as well, signalling that we have an inhomogeneous plane wave. This simply indicates that the direction of phase propagation is not the same as the direction in which the amplitude is attenuated while travelling through the material. Note that t_s is the familiar Fresnel transmission coefficient:[8]

$$t_s = \frac{2n_1 \cos\theta_1}{n_1 \cos\theta_1 + N_2 \cos\theta_2}$$

The blue trace in Figure S1a simulates the distance-dependent mean square electric field profile for an s-polarised beam approaching a diamond or ZnSe (n_1 = 2.4) IRE at 45° with no sample on top. Considering an s-polarised beam is a bit more straightforward as the field is then entirely *y*-polarised, and it is not necessary to decompose the *x*- and *z*-components of the p-polarisation state. Since we are plotting $\langle E_{\text{local}} \rangle^2$ with respect to the incident field (at $z = -\infty$) it is interesting to note that, at the $z = 0^+$ boundary (just inside the refracted medium), the light intensity is roughly 2.5x larger than its incident. However, as the refractive phase is transparent (air), the field for $z > 0$ is evanescent. Its characteristic decay length d_p is given by:[7,9]

$$\frac{1}{d_p} = Im\left[\sqrt{(n_2 + i\kappa_2)^2 - n_1^2 \sin\theta_1^2}\right]$$

We next consider the situation of replacing air with a hypothetical transmitted medium that has the refractive index of water at 3400 cm^{-1} with $n_2 = 1.27$ but no absorption coefficient, and first notice that the field intensity at the boundary is now about 2.7 times larger than its incident value in the prism. (To aid in this comparison, we are not including any reflection losses upon entering the prism.) Furthermore, its decay is also slower, i.e. the so-called evanescent wave penetration depth d_p is longer than it was in air. We next provide the refracted phase with an extinction coefficient in the form of the electric field attenuation coefficient $\kappa = 0.28$ (now fully utilizing the water refractive index at 3400 cm^{-1}). We can see that the resulting purple trace in Figure S1a has a decreased amplitude, but it is challenging to comment on the change of its decay length in this representation due to the differences in the scale. Before returning to this point, we consider one last scenario, that is where the beams approach from air ($n_1 = 1$) rather than from the IRE ($n_1 = 2.4$). Here it is immediately obvious that the surface field is now much smaller, a little more than half of its value just before entering the absorbing refractive medium.

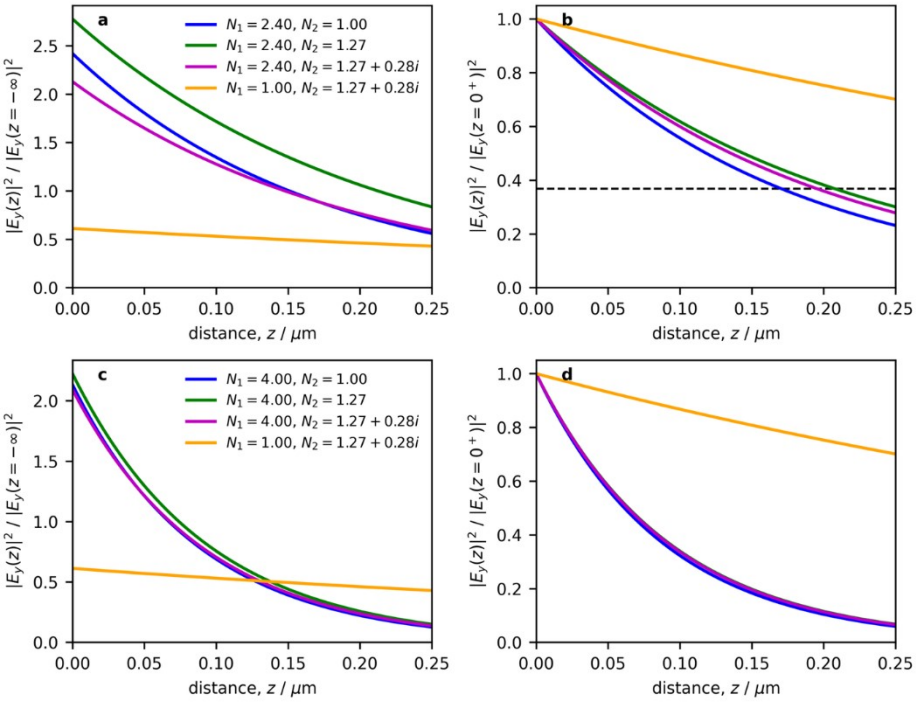

Figure S1. (a,c) Mean squared electric fields as a function of distance with respect to the incident intensity. (b,d) The same data, but normalized with respect to the intensity of fields just on the refracted side of the IRE. Panels A and B show the results for an IRE with $n_1 = 2.4$, such as ZnSe, while C and D show the results for germanium ($n_1 = 4$).

Although this analysis provides valuable information in accounting for the observed absorbance values, it is more insightful to normalize all of these curves with respect to their values at $z = 0^+$, as we have done in Figure S1b. The two cases with transparent

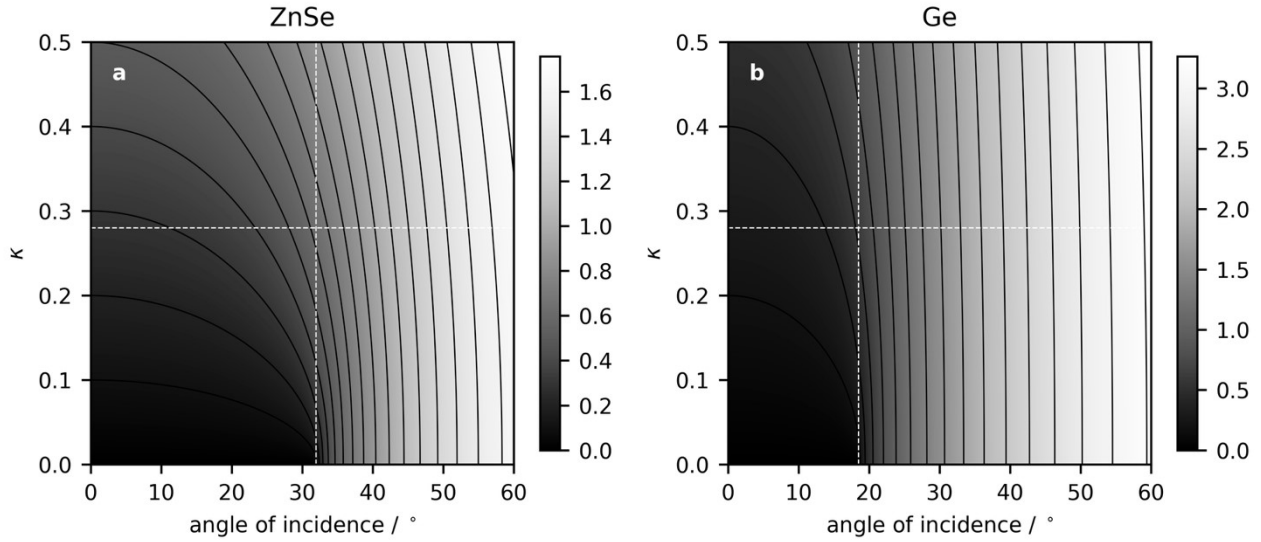

Figure S2. Effective attenuation coefficient as a function of imaginary part of the refractive index κ, and the angle of incidence. The vertical crosshair indicates the critical angle when $\kappa = 0$, and the horizontal crosshair highlights $\kappa = 0.28$ for water at 3400 cm^{-1} with a (a) ZnSe and (b) Ge internal reflecting element.

refracted media are technically not relevant here (no absorption), but it is nevertheless interesting to see how the rate of decay of the electric field into the bulk phase compares with the other cases. In fact, in comparing the green ($n_2 = 1.5$) and blue ($n_2 = 1.27 + 0.28i$) traces, we see that the presence of an absorbing media on the low refractive side of the IRE causes a faster decay of the electric field intensity than was present with an evanescent wave. However, to fully realize the effect of this internal reflection geometry, we also compare with the external reflection case at the same angle (yellow in Figure S1b) to see that the decay is indeed more gradual under external reflection. From this we can conclude that an internal reflection geometry is the most useful for a subsequent weighted subtraction of the bulk water spectrum, as it "concentrates" the electric field within the first micron of the surface. We now repeat these calculations, but change the IRE material to Ge with $n_1 = 4$. The updated mean square fields normalized with respect to the incident intensity (Figure S1c) and with respect to the $z = 0^+$ plane just outside of the IRE (Figure S1d) indicate that the field now decays much more rapidly. This is beneficial either when the absorbance is too high, or when we wish to limit the penetration of the field to the near-surface region. We also note that the penetration depth is much less dependent on n_2 given the high refractive index of Ge.

While it is helpful to look at those specific cases we have described, we can get a unified picture of the effect of field attenuation in absorbing media at different angles of incidence by directly plotting the mean squared field as a function of these two variables in Figure S2. The calculation was again performed using $n_1 = 2.4$, and 1.27 as the real part of the refractive index of the water on top of the ZnSe IRE (Figure S2a). The vertical dashed line at $\theta_1 \approx 38^\circ$ represents the critical angle θ_c when $\kappa = 0$. The first thing to notice is the vertical trend at normal incidence. Here the overall attenuation coefficient has the same value as κ, as one would expect. However, as the angle of incidence increases, the field decays more quickly. Another notable case is the horizontal at $\kappa = 0$ along the bottom edge of the plot. This corresponds to a transparent material in contact with the IRE. Below the critical angle, there is no decay of the field inside the refracted medium (as there is no absorption, and no evanescent wave). Above the critical angle, the evanescent wave penetration depth d_p decreases with increasing angle. Now we can better understand the various cases illustrated in Figure S1, as those are simply combinations depicted along the $\theta = 45^\circ$ vertical line in Figure S2. The transition in behaviour near the critical angle can be seen by the abruptly changing slopes of the equal-attenuation contour lines. The lines are tending towards a vertical orientation for $\theta > \theta_c$, and abruptly rotate so they have very angled profiles for $\theta < \theta_c$, so that they are horizontal at $\theta = 0^\circ$. This calculation was then repeated for the situation where the IRE is made of Ge in Figure S2b. Since the refractive index of Ge is approximately 4, we can see that the critical angle occurs at a much lower angle of incidence. Also note the larger values of the attenuation coefficient (exceeding 3), indicating that the field decays much more quickly inside the water.

In summary, the penetration of the field into the bulk aqueous phase can be limited through a combination of the absorption coefficient and an internal reflection geometry, particularly when the angle of incidence is above what would have been the critical angle if the refracted medium was transparent. When we additionally consider that the absorbance is proportional to the square of the electric field, the decay of the mean squared field is further reduced by an additional factor of two. This enables spectral

features of surface water to have enhanced contrast, essential since the bulk water response dominates the net spectrum prior to the weighted subtraction.

In order to more readily compare the appearance of ATR spectra with spectra recorded in a transmission geometry, one can determine the effective pathlength. This quantity is the thickness of material that would produce the same absorbance in transmission at normal incidence as measured in the ATR configuration at oblique incidence. These expressions take into account the local field enhancement at the interface[10] and result in the plots shown in Figure S3a for ZnSe and Figure S3b for Ge. Since Ge has a shorter penetration depth, and a correspondingly smaller absorbance compared to ZnSe, the corresponding transmission experiment is expected to have a shorter pathlength as demonstrated in Figure S3. Even though the attenuation coefficient and penetration depth is the same for s- and p-polarised light, the effective pathlength is polarisation dependent as the amplitude upon crossing the z=0 IRE-water interface depends on the beam polarisation. If one assumes that the light in the FTIR is randomly polarised, then one can take the average of the s- and p-polarised thicknesses as shown with the dashed line in Figure S3. When multibounce crystals are used, the total effective pathlength is found by multiplying the probing depth with the number of bounces in the ATR crystal.

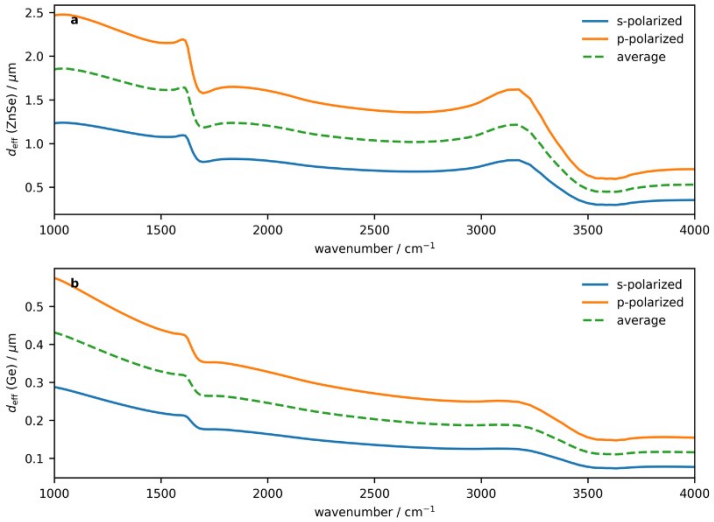

Figure S3 Effective pathlength as a function of frequency for water adjacent to an (a) ZnSe and (b) Ge IRE, showing the result for s-polarised light at 45° (blue), p-polarised at 45° (orange), and their average (green dashed).

Experimental Considerations: Choosing an ATR crystal and geometry

For solutes in solution, the total effective pathlength needs to be selected to the OH stretch is within Beer's law, while still getting the highest possible absorbance of the solute-correlated spectrum. For samples confined to the interface of the ATR crystal, multiple bounces with a shallower probing depth provides a higher surface:bulk ratio, resulting in a larger subtraction factor and correspondingly better signal-to-noise in the final spectrum. Conversely, measuring a second surface pressed against the ATR crystal, such as the membranes discussed in the main text, will benefit from a longer probing depth. For molecular solvation shells, the most important parameter is the total absorbance at the OH stretch and the transparency of the ATR crystal. In our first studies,[11,12] we used a single-bounce diamond ATR crystal. In our recent work,[13–15] we use a multi-bounce germanium (Ge) ATR crystal (Figure S4). This gives rise to an absorption of about 0.6 at the OH stretch of water, which is near ideal, providing a large absorption without causing deviations from Beer's Law, which are expected around an absorption of 1. This multi-bounce trough-type ATR crystal provides much better S/N than single-bounce ATR crystals, but requires about 1 mL to fill, which can be problematic for expensive or custom-synthesized chemicals and biomolecules.

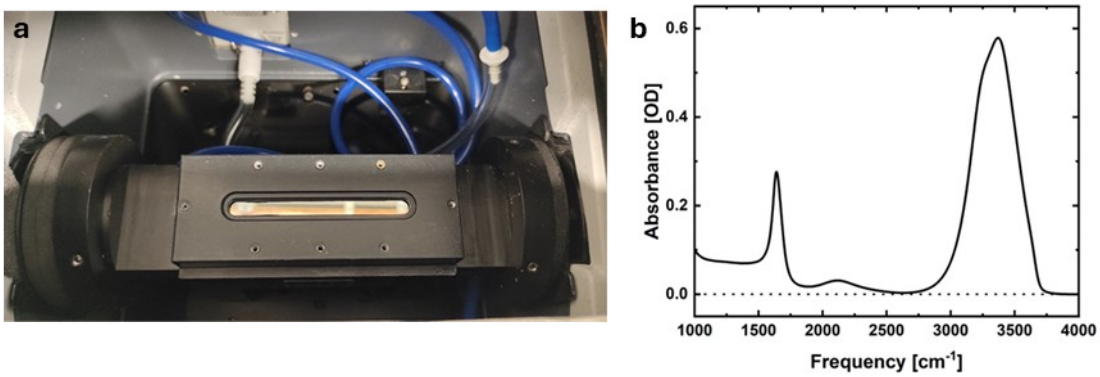

Figure S4: Solvation shell spectroscopy is highly dependent on the choice of ATR crystal. (a) the Horizontal Attenuated Total Reflection (HATR) multi-bounce accessory with a germanium (Ge) crystal, and (b) the spectrum of water obtained using it.

Experimental Methods: Obtaining high quality solvation shell spectra

Solvation shell spectroscopy extracts the small contribution of solvent molecules in the solvation shell from the large background of the bulk solvent. Accordingly, the method requires a high S/N ratio of the solution and solvent spectra to achieve a reasonable S/N ratio in the retrieved spectrum. This is typically not a problem when the solvation shell spectrum is a few percent of the total spectrum, but can be challenge at dilute solutions or for macroscopic surfaces where the solvation shell spectrum can be a fraction of a percent, as illustrated later. As the solvation shell spectrum becomes smaller, minute differences in experimental conditions have a large impact on the quality of the data, so it is critical that the conditions under which the background, solvent, and solution spectra are measured are as constant as possible. This can be achieved through several experimental factors, including purging, cleaning, and careful sample preparation.

Solvation shell spectroscopy is very sensitive to background fluctuations and changes in the atmospheric water and CO_2 content since these can result in significant changes on the scale of the small intensity of the extracted spectrum even though the parent solution and solvent spectra show minimal effects. Care must thus be taken to ensure that the ATR crystal does not move between the reference spectrum and the solution/solvent spectra, which will give rise to background fluctuations, and that the system is well purged to eliminate artifacts from atmospheric absorbances. ATR spectroscopy offers the additional advantage that the beam path can be completely enclosed or even kept in vacuum, and the liquid sample is simply added on top of the ATR crystal without perturbing the beam path, which dramatically reduces problems arising from baseline drifts and changes in the ambient atmosphere.

Nevertheless, a consistent purge of the beam path with clean air, free of water and CO_2, is important, as peaks arising from changes in the atmospheric water and CO_2 content can result in peaks that can be comparable to or larger than the features in the solvation shell spectrum. Changes in the water content will give rise to sharp rotational lines at the OH stretch and OH bend frequencies. While narrow gas phase lines can usually be distinguished from the broader liquid phase spectral features, it can be particularly difficult when capturing the free-OH peak, which falls in the middle of the P and R rotational branches of the atmospheric water. Small changes in the CO_2 content are less detrimental since the CO_2 absorbance around 2350 cm^{-1} usually does not overlap with other spectral features of interest. However, large changes in the CO_2 can give rise to significant spectral changes due to an overtone that appears near the free-OH and can be mistaken for non-hydrogen-bonded water in the solvation shell. The potential artifacts that can arise due to insufficient purge are illustrated in Figure S5. It is important to note the potential for such artifacts to avoid erroneous assignment to free-OH features. While it is, in principle, possible to remove the atmospheric absorption lines, which are well known and can be well-determined in the individual spectrometer, we find it best to avoid additional data processing steps when possible.

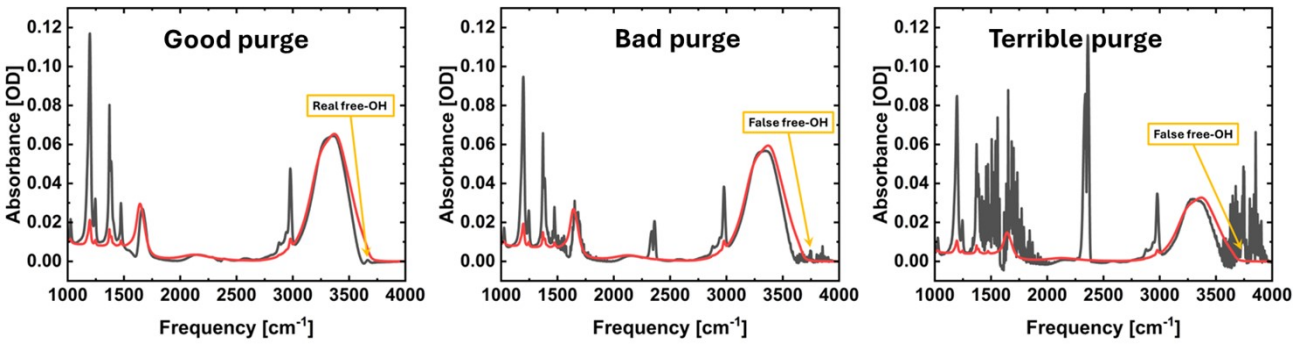

Figure S5: Solvation shell spectroscopy is highly dependent on the choice of ATR crystal. (a) the Horizontal Attenuated Total Reflection (HATR) multi-bounce accessory with a germanium (Ge) crystal, and (b) the spectrum of water obtained using it.

Surface-contaminants: Due to the high surface-sensitivity of ATR spectroscopy, appropriate cleaning of the ATR crystal is critical to get high-quality spectra. Inorganic as well as organic contaminations can easily be adsorbed onto the crystal surface and interfere with the quality of the obtained spectra. To account for different solubilities of various contaminants, the cleaning protocol involves the consecutive washes with three solvents: isopropanol, acetone, and ultrapure water. The order in which these solvents are used is important for effective elimination of the contaminants. Isopropanol and acetone are effective at dissolving most of the nonpolar organic and some inorganic contaminants that are not soluble in water, while the last rinse with ultrapure water ensures that any remaining residues are thoroughly removed. The ATR crystal is rinsed three times with each wash solvent, which is left in contact with the surface for several minutes, before beginning of the measurements.

Bulk contaminants: While bulk contaminants are typically insignificant in the bulk absorbance spectra, they can cause significant artifacts in the subtracted spectra, particularly in the CH stretch region. Simply keeping the ultrapure water in a plastic bottle will lead to CH absorptions from the plastic leaching into the otherwise pure water. Changes in the amount of CH

contaminants between the solution and pure solvent samples gives rise to artificial signals at the CH frequencies in the solvation shell spectrum, which can be either negative or positive depending on the relative amount of contaminants in the parent spectra. This effect is typically insignificant when working at relative high concentrations of the solute, i.e., 1 M of small molecules, but can be significant when operating at dilute concentrations. In our experience, these CH contaminants can obscure the CH stretch range but do usually not affect the rest of the solvation shell spectrum. To obtain the highest quality data possible, we avoid having any of the solutions come in contact with plastic, including plastic pipette tips, and clean all glassware with ALNOCHROMIX™. For more complex solvents, such as buffers or solvent mixtures, it is critical that the solvent in the solution and that of the reference solvent has the identical composition, which is done in these experiments by preparing stock solvent and adding the solutes to a portion of that as required. This procedure enables us to consistently obtain high-quality data.

When applied correctly, it is possible to obtain decent solvation shell spectra even in the presence of large noise. To demonstrate this, we also applied both methods to the 0.1 M TBA measured as a single scan of the interferometer, rather than the usual average of at least 16 scans. This results in a noisier but otherwise equivalent solvation shell as the averaged 0.1 M data, shown in Figure S6, though the artifact around 1500 cm^{-1} causes a vastly under-subtracted initial result.

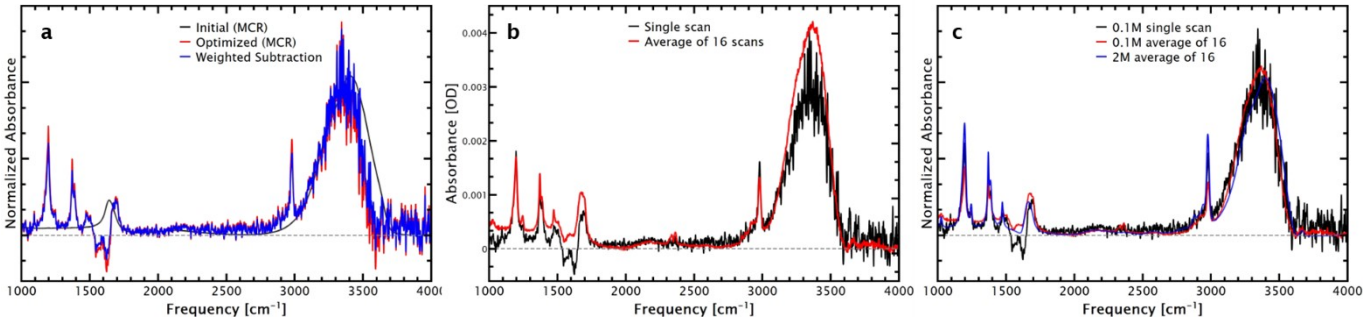

Figure S6: The effects of data quality on the solvation shell spectrum: (a) The MCR and weighted subtraction results for 0.1 M TBA, measured as a single scan of the interferometer. (b) The optimized solvation shell spectra of 0.1 M TBA, measured as a single scan and averaged 16 times. (c) Normalized solvation shell spectra of 2 M TBA, 0.1 M (16 scans), and 0.1 M TBA (single scan).

Data availability

Data for this article, including spectroscopic data, will be made available at the RESOLV data repository.

Acknowledgements

This work was financed by the Deutsche Forschungsgemeinschaft (DFG, German Research Foundation) under Germany's Excellence Strategy EXC2033, project number 390677874 (“RESOLV”) and GRK2376, project number 331085229 (“Confinement-Controlled Chemistry”), as well as the Natural Sciences and Engineering Research Council of Canada, project number RGPIN-2020-06030.

Notes and references

1 M. Moskovits, *J Chem Phys*, 1982, **77**, 4408–4416.
2 U. P. Fringeli and H. H. Günthard, *Mol Biol Biochem Biophys*, 1981, **31**, 270–332.
3 N. Kumaran, C. L. Donley, S. B. Mendes and N. R. Armstrong, *Journal of Physical Chemistry C*, 2008, **112**, 4971–4977.
4 W. N. Hansen, *JOSA,* 1968, **58***,* 380–390.
5 K. Yamamoto and H. Ishida, *Applied Spectroscopy,* 1994, **48**, 775–787.
6 E. G. Moloney, Md. S. Azam, C. Cai and D. K. Hore, *Biointerphases*, 2022, **17**, 051202.
7 N. J. Harrick, *Internal Reflection Spectroscopy*, John Wiley & Sons, New York, 1967.
8 M. Born, E. Wolf, A. B. Bhatia, P. C. Clemmow, D. Gabor, A. R. Stokes, A. M. Taylor, P. A. Wayman and W. L. Wilcock, *Principles of Optics*, Cambridge University Press, Cambridge, 7th Ed., 2020.
9 M. Milosevic, *Internal Reflection and ATR Spectroscopy*, 2012, **176**, 1–258.
10 L. A. Averett, P. R. Griffiths and K. Nishikida, *Anal Chem*, 2008, **80**, 3045–3049.
11 Y. Sun and P. B. Petersen, *J. Phys. Chem. Lett.* 2017, **8**, 611–614.
12 C. A. Daly, L. M. Streacker, Y. Sun, S. R. Pattenaude, A. A. Hassanali, P. B. Petersen, S. A. Corcelli and D. Ben-Amotz, *J. Phys. Chem. Lett*. 2017**, 8**, 5246–5252.
13 E. Casalini, A. M. Stingel, B. Moussa, M. Personeni, P. B. Petersen and A. Vila Verde, *JACS Au*, 2025, **5**, 2992–2999.

14 H. Geraili Daronkola, B. Moussa, Ó. Millet, O. Krenczyk, G. Ortega-Quintanilla, P. B. Petersen and A. Vila Verde, *Protein Science*, 2025, **34**, e5241.
15 S. Karla, M. Sorci, B. Moussa, R. Banik, P. B. Petersen, J. Plawsky and G. Belfort, *J Colloid Interface Sci*, 2026, **701**, 138530.